Original Article

Physical-metallurgical properties and micro-milling machinability evaluation of high entropy alloy FeCoNiCrAl$_x$

Xiaoliang Liang, Chunjin Wang[*], Canbin Zhang, Chi Fai Cheung[**]

State Key Laboratory of Ultra-Precision Machining Technology, Department of Industrial and Systems Engineering, The Hong Kong Polytechnic University, Kowloon, Hong Kong, China

ABSTRACT

High-entropy alloy (HEA) belongs to the emerging multi-principal alloy with excellent mechanical-physical properties. The material machinability is critical for cutting planning, especially for novel materials with various chemical compositions and mechanical properties. The machinability of high-entropy alloys mainly depends on the physical-metallurgical properties and cutting conditions. This work investigated the physical-metallurgical properties and micro-machinability of HEA FeCoNiCrAl$_x$ (x = 0.1, 0.5, 1) with vacuum arc melting preparation. Experimental results indicated that the difference of Al element content affected the chemical element distribution, phase composition, microstructure, and microhardness of prepared HEA FeCoNiCrAl$_x$. FeCoNiCrAl$_{0.1}$ appeared single face-center-cubic (FCC) structure, while the increase in Al element content led to dual face-center-cubic and body-center-cubic (FCC + BCC) structure for FeCoNiCrAl$_{0.5}$ and FeCoNiCrAl$_1$. The average microhardness values were approximately 183 HV, 294 HV, and 461 HV for FeCoNiCrAl$_{0.1}$, FeCoNiCrAl$_{0.5}$, and FeCoNiCrAl$_1$, respectively. The increase in Al element content led to poor material machinability, in which FeCoNiCrAl$_{0.1}$ had better machinability due to lower micro-milling forces, more stable cutting process, lower specific cutting energy, better surface qualities and smaller tool wear. This work combined the prepared material properties and micro-machinability evaluation to guide HEA design and select practical machining parameters.

© 2022 The Author(s). Published by Elsevier B.V. This is an open access article under the CC BY-NC-ND license (http://creativecommons.org/licenses/by-nc-nd/4.0/).

1. Introduction

In the traditional alloy design, the material performance largely depends on the single element solubility limit and phase ratio. However, the multi-principal high-entropy alloy (HEA) breaks through the traditional multi-element alloy design concept, which generally consists of 5–13 main elements such as Al, Ti, V, Cr, Mn, Fe, Co, Ni, Cu, Zn, Mo and W with each element molar content between 5%~35% [1]. Due to the multi-principal elements characteristics, HEA exhibits various excellent features superior to conventional

---

intermetallic compounds, for instance high strength, good wear resistance, high-temperature oxidation, corrosion resistance, and high resistivity, etc [2,3]. HEA is possible to make a large application of high-strength high-temperature corrosion-resistant tools, molds, and machines. However, it has not been widely used currently due to the complexity and high cost of preparation process.

Many researchers have focused on the preparation methods and physical-metallurgical properties of HEA. Currently, HEA is mainly fabricated by vacuum melting, powder metallurgy, mechanical alloying, laser molten, electrochemical deposition method [4–8]. Each preparation method has its benefits and shortcomings. According to the element composition and application fields of HEA, the preparation method, process and performance are the keys to develop. Among them, the vacuum melting method has been used by most researchers to prepare HEA. Soare et al. [9] prepared multi component HEA AlCrCuFeMnNi by vacuum induction melting, and also studied the microstructure, mechanical properties, and corrosion characteristics after the remelting process. Sun et al. [10] fabricated the multi-principal element alloys $Al_xFeCoNiCu/TiC$ with different Al element contents from Al–Fe–Co–Ni–Cu–Ti–C systems by vacuum inductive melting, and also analyzed microstructure and mechanical property. Zhang et al. [11] prepared the equimolar refractory HEA NbZrTiCrAl by vacuum arc melting, and studied the microstructure and oxidation response at 800 °C, 1000 °C and 1200 °C. Wang et al. [12] prepared HEA $AlCoCrCuFeNi_x$ by melting WK-type non-consumable vacuum melting furnace under the protection of argon, and also studied the as-cast microstructure, phase structure and hardness. Jiang et al. [13] focused on the effect of W element on microstructure and room temperature mechanical behavior of HEA $CrFeNi_2V_{0.5}W_x$ ($x = 0$, 0.25). Their compressive testing results indicated that the $CrFeNi_2V_{0.5}W_{0.25}$ had better yield strength than that of W-free $CrFeNi_2V_{0.5}$. There were certain differences in the microstructure and mechanical properties of HEA, and high reproducibility has not been achieved. The basic premise to be industrialized was that materials with stable structure and performance could be fabricated through certain preparation methods.

The application of HEA for precision manufacturing components usually requires machining process. The material machinability is critical for process planning. Especially for novel materials with various chemical compositions and mechanical properties, the machinability was the main criterion for materials selection. Most of the existing literatures focused on the machinability of HEA during the primary manufacturing process. Guo et al. [14] investigated the machinability of selective laser melting HEA CoCrFeMnNi with milling, polishing, and grinding processes, which studied preliminary machinability evaluation considering surface topography, elemental compositions, microhardness, residual stresses and subsurface microstructure. Clau et al. [15] analyzed the influence of cutting speeds on the surface properties during turning thermally sprayed HEA AlCoCrFe-NiTi layers by atmospheric plasma spraying, which addressed deeper understanding of the cutting mechanisms. Liborius et al. [16] investigated the effects of cutting tool materials on tool wear, surface roughness, and cutting forces components

for different cutting speeds in turning HEA CoCrFeNi. Litwa et al. [17] provided the cutting characteristics of HEA CrMnFeCoNi by selective laser melting processes, which indicated that CrMnFeCoNi had better machinability than AISI 304L steel in terms of surface quality and tool wear. Constantin et al. [18] estimated the machinability of HEA $Al_{0.6}CoCrFeNi$ considering cutting speeds, material removal rates and tool life. They pointed out that the expanded range of cutting parameters for fine cutting was premeditated to optimize cutting parameters. Huang et al. [19] investigated the machinability of HEA $Al_{80}Li_5Mg_5Zn_5Cu_5$ during ultra-precision cutting with diamond tools, which exhibited small tool wear and good surface roughness after cutting process. Richter et al. [20] focused on the effects of cutting speeds and feed rates on the machinability of HEA CoCrFeMnNi including cutting forces, surface topography and microstructure during ball end milling.

Since the expanding application range of micro cutting technology, micro components have been widely used in industrial fields such as national defense, aerospace, precision engineering, biotechnology, and communications [21,22]. Micro-milling process technology had the comprehensive advantages of strong system rigidity, good adaptability, outstanding manufacturing capability, high efficiency and low cost, and it has always been the research hotspot. Because the uncut chips thickness in the micro-milling was smaller, and the specific value of uncut chips thickness to the cutting edge radius was much higher [23]. The removal mechanisms from ploughing to shearing transitions were determined by the chips thickness in relation to the cutting edge radius [24,25]. Therefore, the cutting mechanisms in micro-milling are distinct from the macro-milling in some aspects, and the size effect makes it more complicated.

Since the machinability mainly depends on the material properties and cutting conditions, this work investigated the physical-metallurgical properties and micro-machinability of HEA $FeCoNiCrAl_x$ ($x = 0.1$, 0.5, 1) with vacuum arc melting preparation. On the one hand, the chemical elements, phase composition, microstructure, and microhardness of the prepared HEA $FeCoNiCrAl_x$ were compared. On the other hand, the micro-milling machinability of HEA $FeCoNiCrAl_x$ were analyzed according to cutting force, specific cutting energy, cutting stability, surface qualities, chips morphology, and tool wear. This work can help guide HEA designs and select cutting parameters.

2. Experimental methods

2.1. High-entropy alloy preparation process

The HEA $FeCoNiCrAl_x$ samples used in the experiments were all self-fabricated by vacuum arc melting. According to the determination and weighing 99.9 wt.% high-purity elements of iron (Fe), cobalt (Co), nickel (Ni), chromium (Cr), and aluminum (Al) powder metal raw materials to ensure chemical uniformity. The raw materials were smelted into 1650 °C under the protection of argon gas. The melting process adopted the magnetic stirring method, and the uniformity of the samples was ensured by remelting 5 times. Hence, the

samples were homogenized at 1200 °C for 5 h to obtain solid solution alloy. Electrical discharge machining (EDM) was used to cut the experimental samples into the size of 10 mm × 10 mm × 2 mm, and the EDM heat-affected layer was removed by grinding and polishing processes.

2.2. Experimental design

Fig. 1 presents the micro-milling experimental device, the micro-milling tool appearance, and surface micro-channels. The experiment was conducted on a five-axis ultra-precision machining center (Toshiba UVM-450C) under the dry cutting environment. Before starting micro-milling process, the dynamic balance of the spindle was adjusted. The micro-milling tool Mugen-coating premium NS MXH230 Micro Tool with 2 flutes, 30° helix angle, and cutting edge radius 1.2 μm was used. The cutting forces were measured by Kistler 9256C1 piezoelectric dynamometer, and the loads from three-axis were connected to its acquisition program. Table 1 lists the micro-milling parameters. The length of each micro-channel was 10 mm, and the width was equal to the diameter of the micro-milling tool. When machining each micro-channel, the feed direction of the micro-milling tool was kept the same.

2.3. Testing method

The HEA samples were embed in the conductive mounting powder by using the mounting machine (XQ-2B), and then ground and polished by sandpaper and flannel. The microstructure was obtained by immersing the samples in aqua regia (30 ml HCl + 10 ml HNO_3) for chemical etching of 2 s. The microstructure was observed under HITACHI S3000H scanning electron microscope equipped with EDS analysis attachment. The phase compositions were evaluated by D8 ADVANDC X-ray patterns. The microhardness measurement was completed by Vickers micro-indentation hardness testing. The microhardness at random ten positions were

Table 1 – Experimental parameters of micro-milling process.

Materials	Spindle speed S (r/min)	Feed rate f (mm/min)	Feed per toolth f_z (μm/z)	Axial depth of cut a_p (μm)
$FeCoNiCrAl_x$	60,510	60, 120, 360	0.6, 1.8, 3	0.075

measured to determine the average microhardness of HEA $FeCoNiCrAl_x$. After the micro-milling experiment process, the three-dimensional (3D) machined surface was measured by laser microscope. The machined surface defects, edge burrs, chips morphology and tool wear were examined by scanning electron microscope.

3. Results and discussions

3.1. Physical-metallurgical properties

3.1.1. Element distribution analysis

The difference Al element content affected the element distribution, phase composition, microstructure, and microhardness of HEA $FeCoNiCrAl_x$. Fig. 2 shows the element composition and distribution analysis of different Al element content of HEA $FeCoNiCrAl_x$. The actual element composition ratio of $FeCoNiCrAl_x$ were very close to the nominal composition, indicating that there was no obvious element composition change during vacuum arc melting preparation process. Moreover, the element distribution of $FeCoNiCrAl_{0.1}$ was relatively uniform with less element segregation. However, $FeCoNiCrAl_{0.5}$ and $FeCoNiCrAl_1$ had obvious element segregation during the solidification process because the mixing enthalpy between Al–Ni was not conducive to the formation of solid solution. As a result, the element segregation occurred and the intergranular Al–Ni phase was
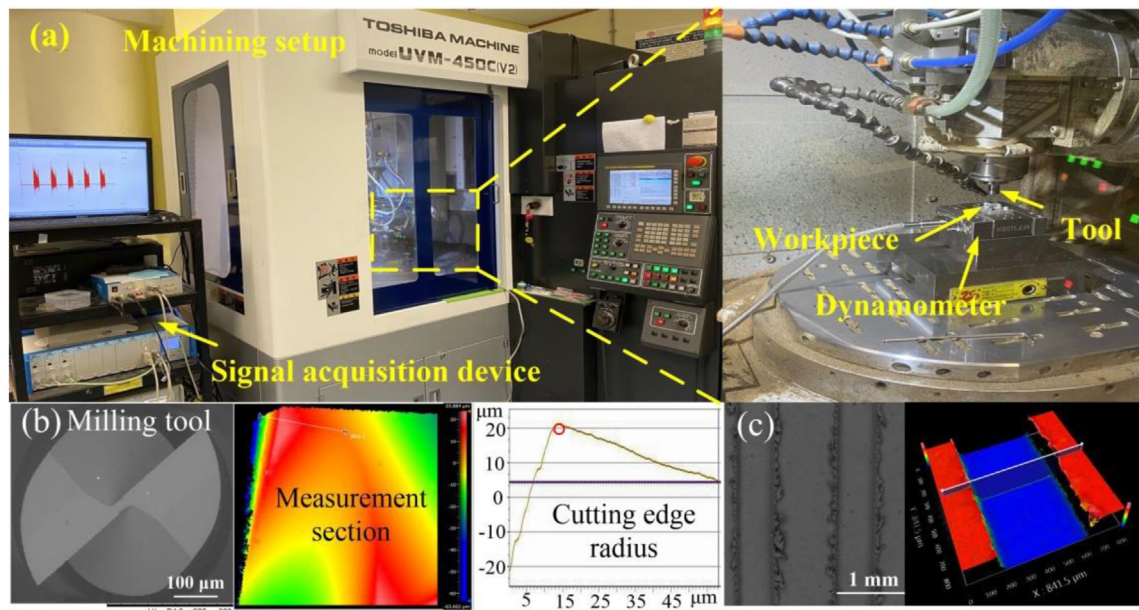

Fig. 1 – Machining setup, (a) micro-milling experimental device, (b) micro-milling tool appearance, (c) micro-channels.
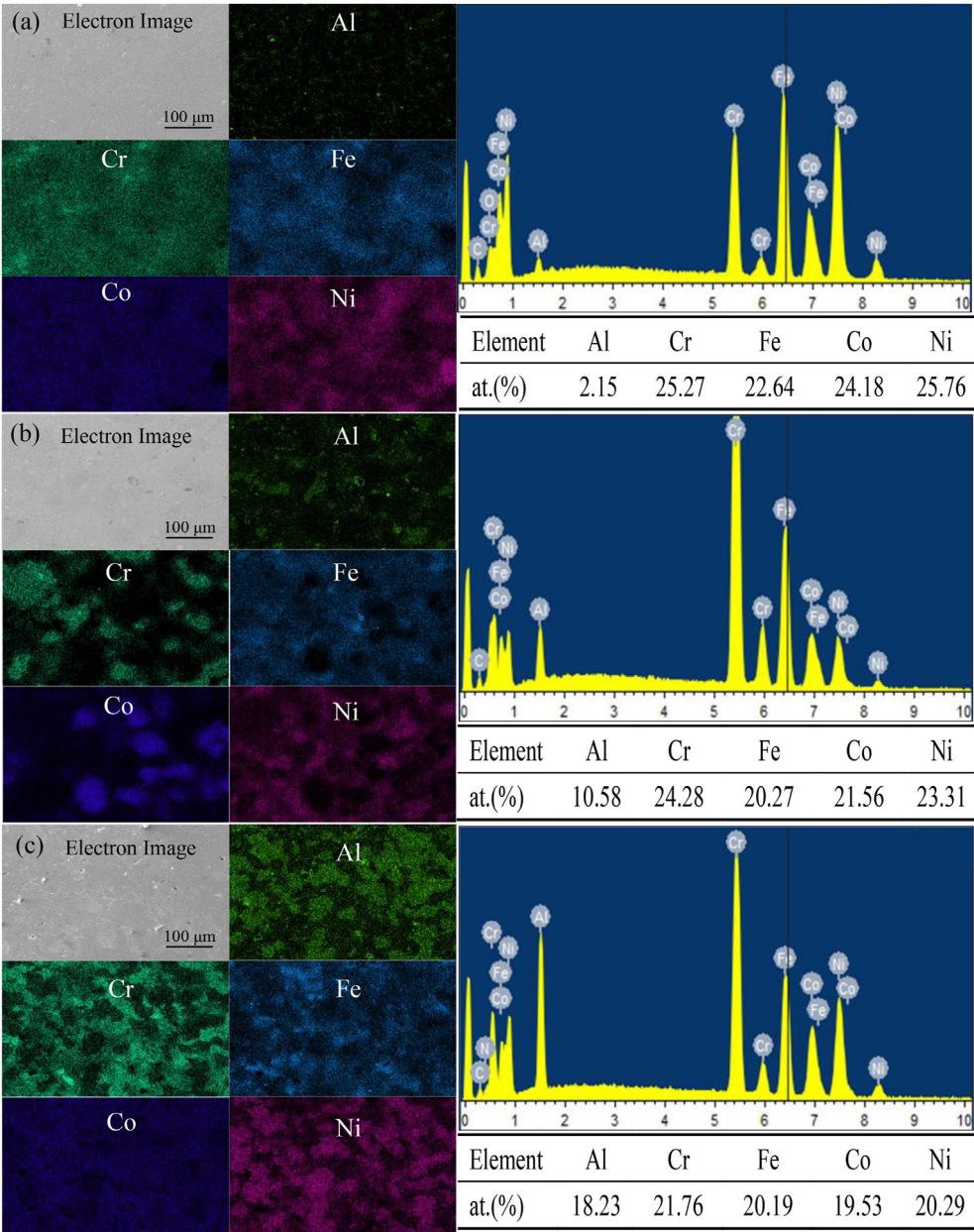
Fig. 2 – Element composition and distribution analysis of HEA FeCoNiCrAl$_x$, (a) FeCoNiCrAl$_{0.1}$, (b) FeCoNiCrAl$_{0.5}$, (c) FeCoNiCrAl$_1$.

formed, which resulted in the relatively large elements Fe, Co, and Cr solidifying intergranular phase.

3.1.2. Phase composition and microstructure

Fig. 3 presents the typical phase compositions of HEA FeCoNiCrAl$_x$. The low Al element content of FeCoNiCrAl$_{0.1}$ had a single face center cubic (FCC) structure. Such result was consistent with the EDS analysis, which FeCoNiCrAl$_{0.1}$ exhibited relatively uniform element distribution proving the single-phase structure. With the increase of Al element content, the coexistence of dual structure (face center cubic and body center cubic, FCC + BCC) began to appear. The BCC structure appeared at the diffraction angle 44.6° for FeCoNiCrAl$_{0.5}$. The increase in Al element content also led to

a corresponding intensity enhancement of BCC structure. Not only did the intensity increase at the diffraction angle of 44.6° for FeCoNiCrAl$_1$, but a new peak of the BCC structure appeared at the diffraction angle of 82.1°. According to the relative peak intensity in the XRD curve, the proportion of the BCC phase in the HEA FeCoNiCrAl$_x$ became higher with the increase of Al element content, which proved that the Al element played a role as the BCC forming element in the HEA.

As shown in Fig. 4, the microstructure of HEA FeCoNiCrAl$_x$ was obtained by SEM analysis. According to the microstructure, it was seen that although the atomic radii of Al atoms was different from other elements, the significant phase separation was not appeared in the FeCoNiCrAl$_{0.1}$,
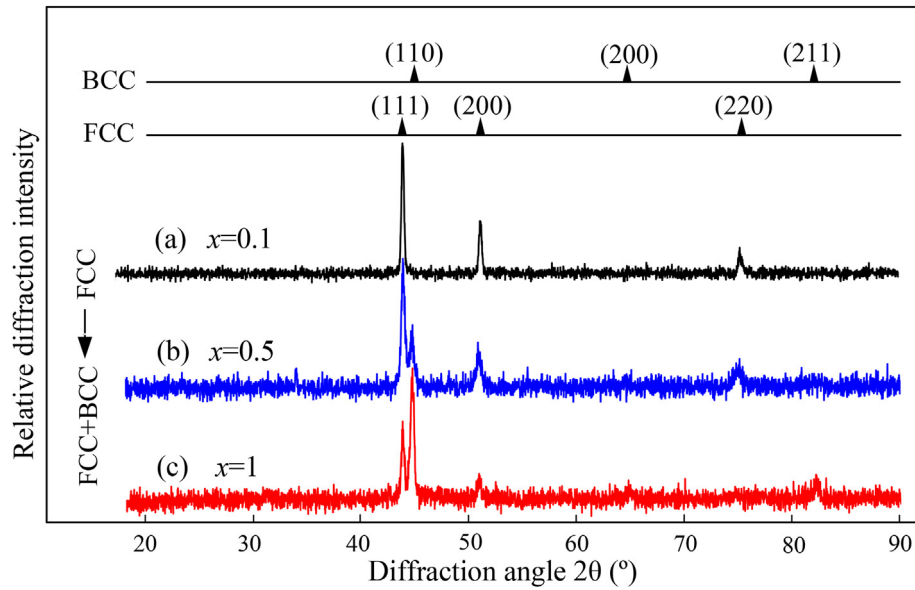
Fig. 3 − XRD pattern of HEA FeCoNiCrAl$_x$, (a) FeCoNiCrAl$_{0.1}$, (b) FeCoNiCrAl$_{0.5}$, (c) FeCoNiCrAl$_1$.

thus forming a uniform solid solution. The equiaxial microstructure morphology was seen in FeCoNiCrAl$_{0.1}$. Such microstructure morphology was identified as FCC phase with XRD analysis. The increase of Al element content caused the microstructure of HEA FeCoNiCrAl$_x$ changed, which generated the gray and white fission biphasic microstructure. Corresponding to the element distribution results, the BCC phase with an irregular network structure

riching in elements Al and Ni was precipitated on the FCC matrix.

3.1.3. Microhardness

The microhardness of HEA FeCoNiCrAl$_x$ was affected by the different microstructures through adjusting Al element content. As shown in Fig. 5(a), the microhardness of FCC phase was about 183 HV while the microhardness of BCC
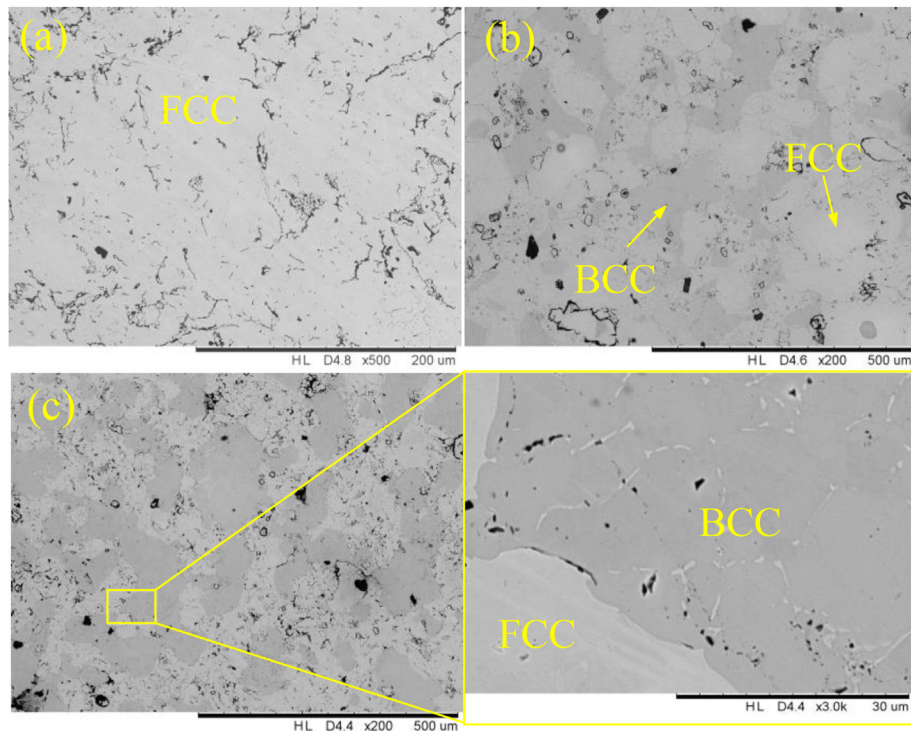

Fig. 4 − Microstructure of HEA FeCoNiCrAl$_x$, (a) FeCoNiCrAl$_{0.1}$, (b) FeCoNiCrAl$_{0.5}$, (c) FeCoNiCrAl$_1$.
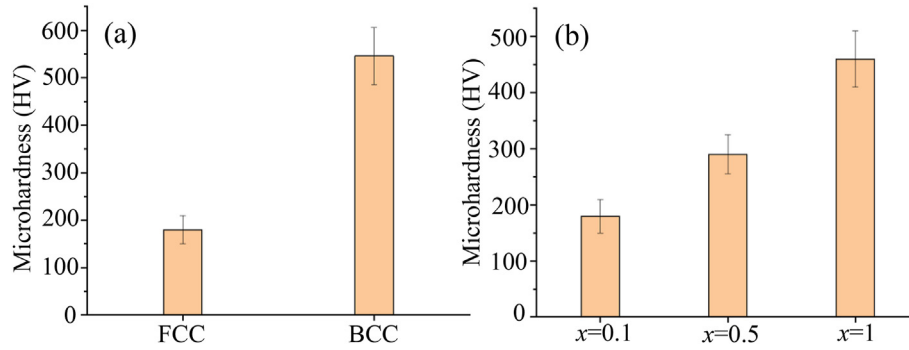
Fig. 5 − Microhardness analysis of HEA FeCoNiCrAl$_x$, (a) FCC and BCC, (b) average microhardness value.

phase was about 546 HV under the condition of HEA FeCoNiCrAl$_1$. Such result indicated that the microhardness of BCC phase was higher than that of FCC phase. As shown in Fig. 5(b), the average microhardness value of FeCoNiCrAl$_{0.5}$ and FeCoNiCrAl$_1$ were approximately 294 HV and 461 HV, respectively. This was caused by that the HEA had an FCC structure under the condition of FeCoNiCrAl$_{0.1}$ while FCC structure gradually transformed into BCC structure for FeCoNiCrAl$_{0.5}$ and FeCoNiCrAl$_1$. The overall change in the

microhardness of FeCoNiCrAl$_x$ was consistent with the fraction of the BCC structure.

3.2. Micro-milling machinability

3.2.1. Cutting forces, cutting stability and specific cutting energy

Generally, cutting force was one of the important factors for evaluating material machinability. Fig. 6 shows the change
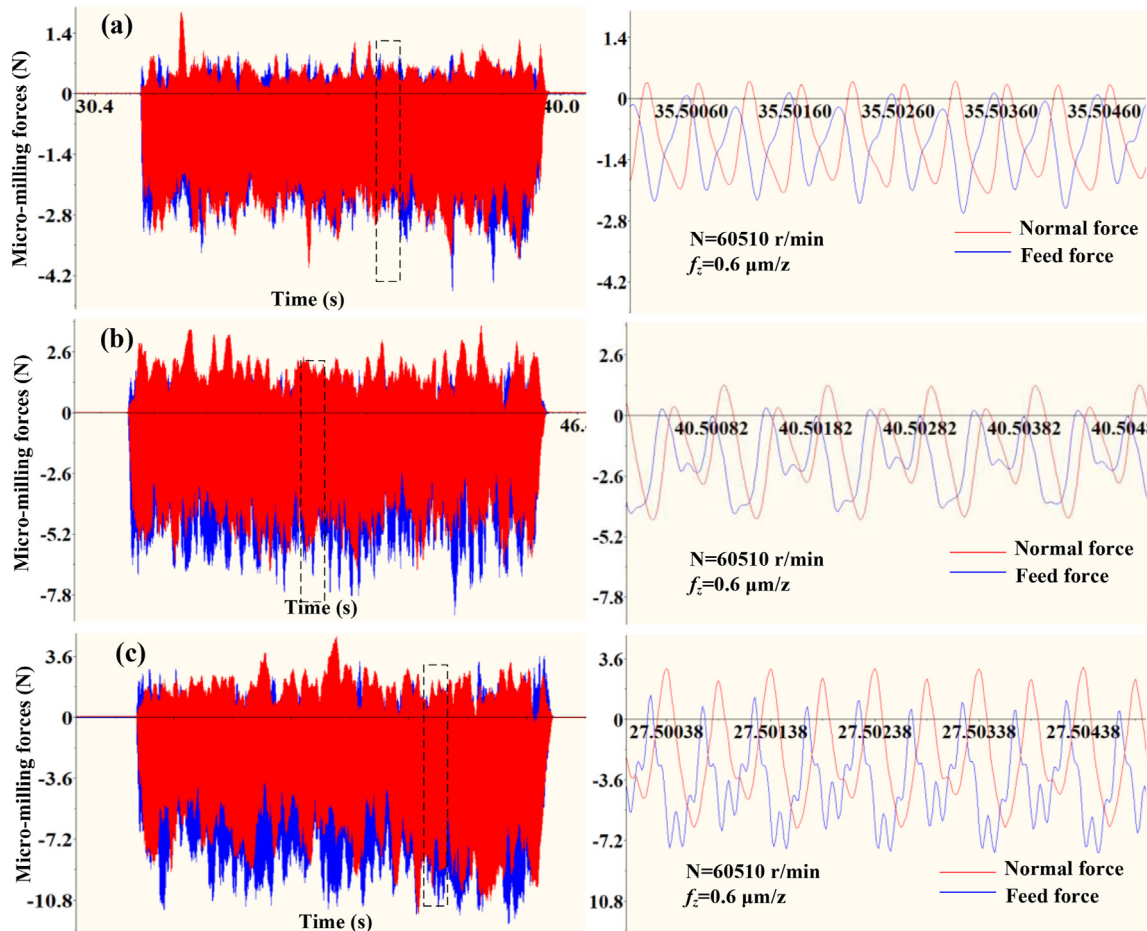

Fig. 6 − Micro-milling forces in feed and normal directions under the condition of 0.6 μm/z, (a) FeCoNiCrAl$_{0.1}$, (b) FeCoNiCrAl$_{0.5}$, (c) FeCoNiCrAl$_1$.

trend of feed force (F_x) and normal force (F_y) of HEA FeCoNiCrAl$_x$ under the condition of feed per tooth 0.6 μm/z. On the one hand, the periodic change of cutting forces during the micro-milling process was related to the intermittent down milling and up milling processes. On the other hand, it was possible that the whole impact originated from the energy expended by cutting, friction, and material deformation for different HEA FeCoNiCrAl$_x$. Experimental results also indicated that the micro-milling forces increased with the increase of Al element content. Compared with FeCoNiCrAl$_{0.1}$, the normal component forces increased by 112.3% and 261.1%, while the feed component forces increased by 45.6% and 159.8% for FeCoNiCrAl$_{0.5}$ and FeCoNiCrAl$_1$, respectively. This trend was consistent with the expected result that the HEA FeCoNiCrAl$_x$ has higher strength and microhardness with the increase of Al element content, therefore exhibiting higher micro-milling forces [26].

Fig. 7 analyzes the variation trend of feed force (F_x) and normal forces (F_y) under different micro-milling parameters. Under all micro-milling parameter conditions, the cutting force components in the feed direction were greater than that of the normal direction. Moreover, experimental results showed that the cutting force components overall increased with the increase of feed rate. When the micro-milling feed rate changed from 0.6 μm/z to 3 μm/z for FeCoNiCrAl$_{0.1}$, FeCoNiCrAl$_{0.5}$, and FeCoNiCrAl$_1$, the normal component forces increased by 29.8%, 16.1%, and 31.5%, and the feed component forces increased by 50.9%, 43.9%, and 52.6%, respectively. Such result indicated that although the micro-milling feed rate increased proportionally, the cutting force components increased by the disproportionate multiple. This phenomenon was mainly because when the uncut chips thickness was smaller than cutting edge radius, the ploughing effect was more obvious, and the chips were not easy to generate resulting in more friction.

The energy consumption of the micro-milling process influences the environment and industrial costs. The specific cutting energy belongs to a critical metric for determining the effectiveness of micro-milling process, which is calculated by Eq. (1). As shown in Fig. 8, the size effects of micro-milling process were directly detected. The specific cutting energy rose nonlinearly when the feed rate was reduced, which the specific cutting energy under the feed per tooth 0.6 μm/z increased by 326.2%, 335.6%, and 227.6% than that of 3 μm/z for FeCoNiCrAl$_{0.1}$, FeCoNiCrAl$_{0.5}$, and FeCoNiCrAl$_1$, respectively. When the feed rate smaller than the cutting edge radius, this tendency was owing to the impacts of negative rake angle resulted in higher material deformation, which the uncut chips were hard to remove from the workpiece. Under the condition of high feed rate, shear effect became the main removal mechanism in the micro-milling process, which the specific cutting energy was much smaller than that of the ploughing dominated range. Moreover, the specific cutting energy of HEA FeCoNiCrAl$_x$ increased with the increase of Al element content. Especially the specific cutting energy of FeCoNiCrAl$_1$ increased by 152.2%, 115.6%, and 229.8% than that of FeCoNiCrAl$_{0.1}$, under the condition of 0.6 μm/z, 1.8 μm/z, and 3 μm/z, respectively. Such result was associated with higher microhardness of FeCoNiCrAl$_1$ dissipating higher energy to separate from workpiece during the micro-milling process.

$$h_{uncut} = f_z \cdot a_e / [r \cdot \arccos(1 - a_e/r)]$$
$$U = \sqrt{Fx^2 + Fy^2} \cdot v \Big/ (h_{uncut} \cdot a_p \cdot v) \tag{1}$$

where h_{uncut} represents the average uncut chips thickness. a_e represents the radial depth of cut. r is the milling tool radius. U is the specific cutting energy. v is cutting speed.

The cutting forces for frequency domain analysis was calculated by Fast Fourier transform (FFT) method to evaluate the cutting stability. As shown in Fig. 9, the frequencies of feed cutting force components included spindle frequency (SF), tool-passing frequency (TPF), and their multiples frequency signals (2 PF). It was seen that the frequency peak amplitude increased with the decrease of feed rate, which mean the cutting process gradually tended to be unstable. Such trend was related to the ploughing effect causing cutting instability. Therefore, accordingly increasing the feed per tooth could improve cutting stability. In addition, a large
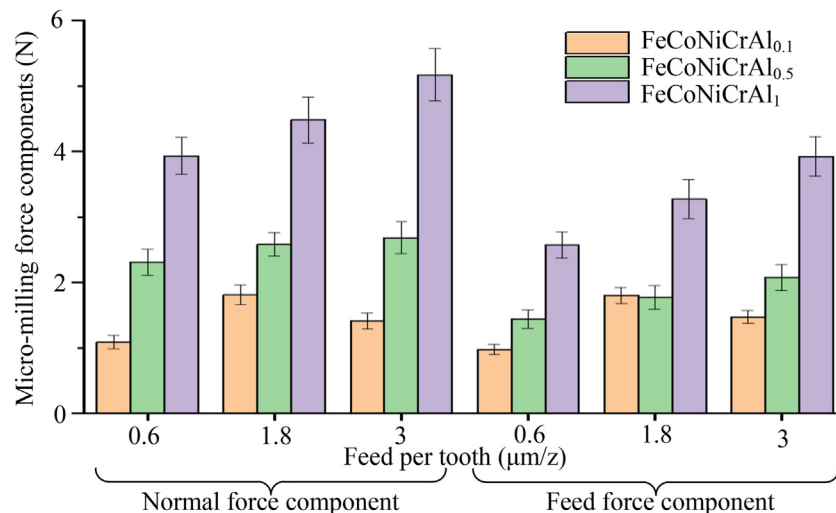

Fig. 7 – Cutting force components analysis under different micro-milling parameters.
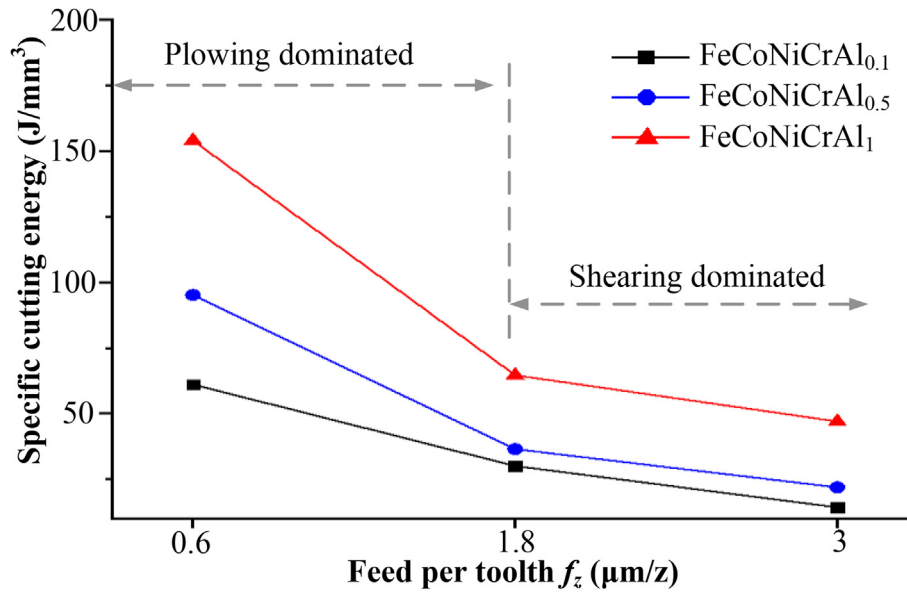
Fig. 8 − Specific cutting energy analysis under different micro-milling parameters.

peak at the tool-passing frequency enhanced with the increase of Al element content. Such result indicated that higher Al element content of HEA FeCoNiCrAl$_x$ resulted in the cutting unstable, the tool tip jumping, and the chips loads redistributed uneven [27,28].

3.2.2. Surface topography

Fig. 10 presents the 3D machined surface topography of the micro-channels under various micro-milling parameters. The results showed that the surface topography had high precision throughout the micro-milling process, indicating that the
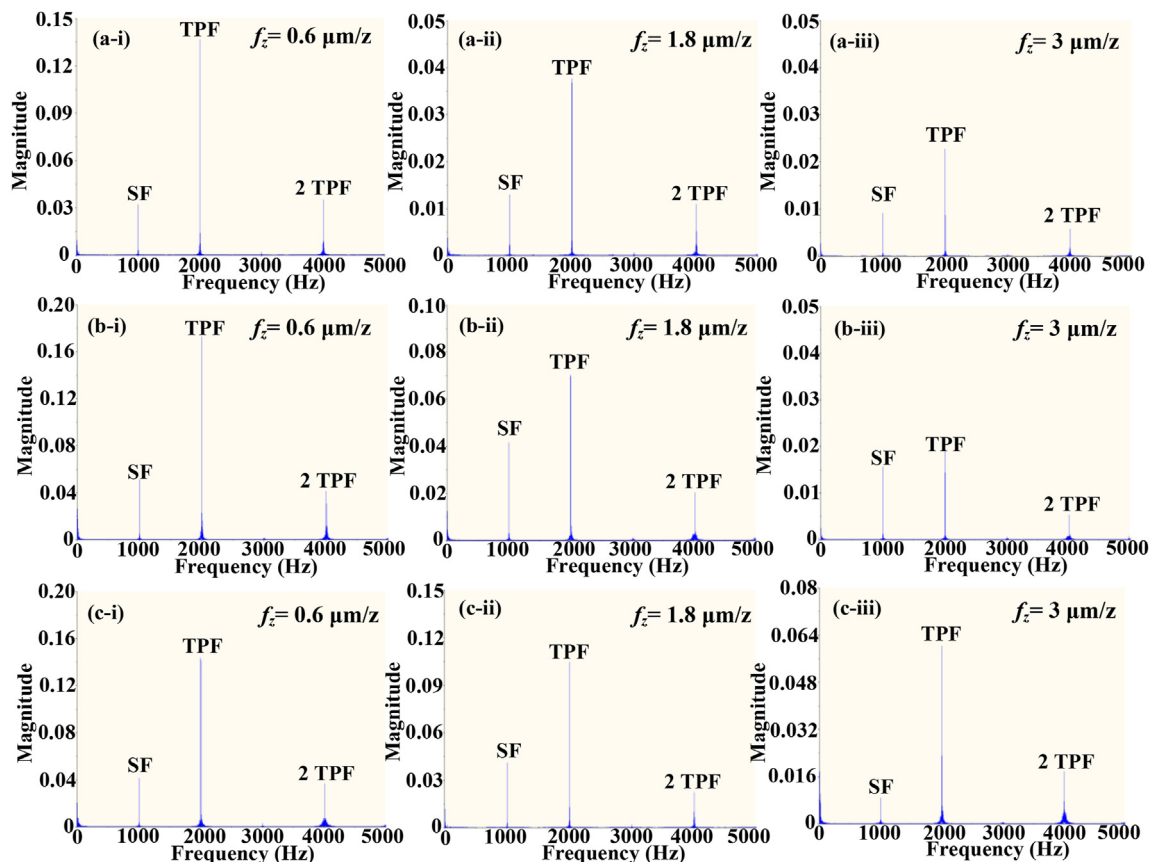

Fig. 9 − Fast Fourier transforms analysis of feed force components, (a) FeCoNiCrAl$_{0.1}$, (b) FeCoNiCrAl$_{0.5}$, (c) FeCoNiCrAl$_1$.
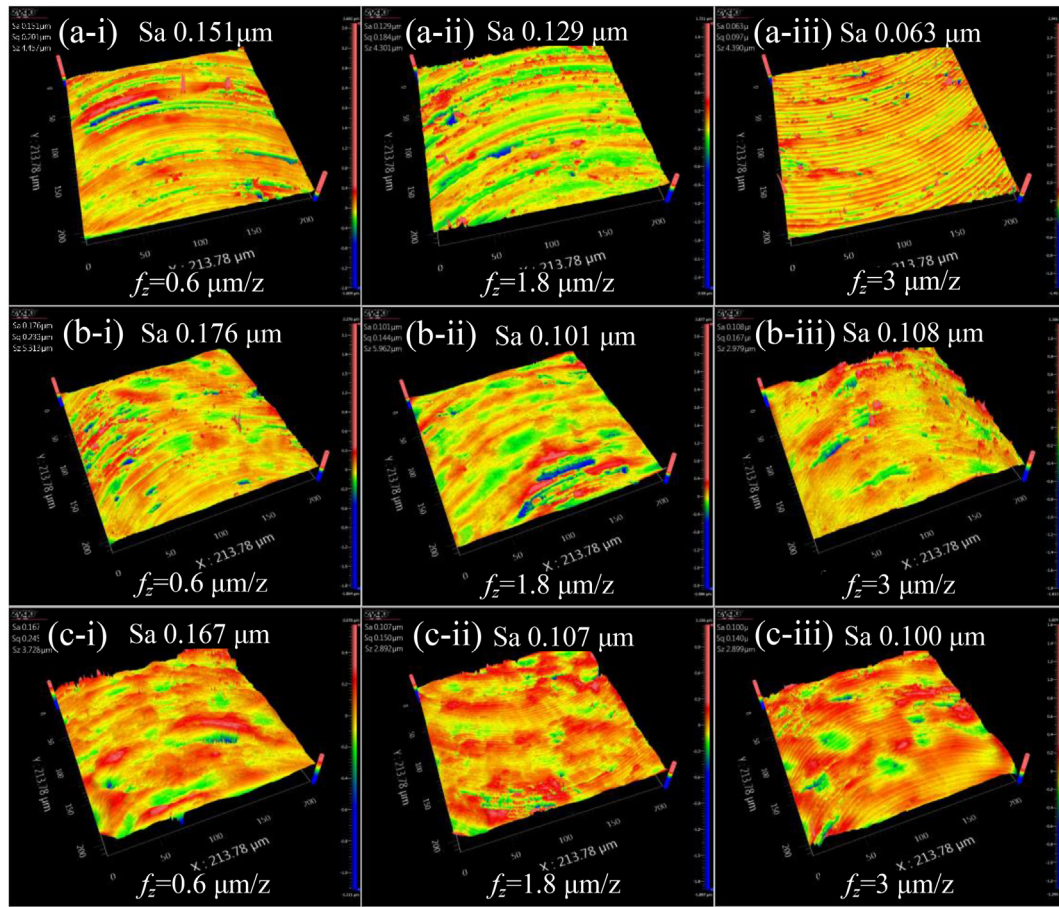
Fig. 10 − 3D machined surface topography after micro-milling process under different feed rates, (a) FeCoNiCrAl$_{0.1}$, (b) FeCoNiCrAl$_{0.5}$, (c) FeCoNiCrAl$_1$.

coated cemented carbide micro-milling tools could easily remove HEA FeCoNiCrAl$_x$, especially the machined surfaces of lower Al element content FeCoNiCrAl$_{0.1}$ obtained better surface quality. A certain degree of feed marks could still be seen from the 3D machined surface topography. Due to the squeezing and ploughing effects of the cutting edge, the machined surfaces were accompanied by a certain degree material plastic smearing under the condition of lower feed rate.

Fig. 11 presents the surface roughness in surface average mean height Sa of the middle of the micro-channels under different micro-milling parameters. The machined surface with higher Al element content generally appeared worse surface roughness, which could be explained by more surface defects due to higher microhardness and brittleness during the micro-milling process [29]. Especially surface roughness Sa of FeCoNiCrAl$_1$ increased by 23.2%, 11.3%, and 46.8% than that of FeCoNiCrAl$_{0.1}$ under the condition of 0.6 μm/z, 1.8 μm/z, and 3 μm/z, respectively. Moreover, the reduction in the feed rate resulted in higher surface roughness in case of the feed rate was smaller than cutting edge radius. Compared with the condition of 0.6 μm/z, surface roughness Sa decreased by 23.2%, 11.3%, and 46.8% under the condition of 3 μm/z for FeCoNiCrAl$_{0.1}$, FeCoNiCrAl$_{0.5}$, and FeCoNiCrAl$_1$, respectively. Such trend could be explained by the ploughing phenomenon dominating cutting instability and uneven material plastic flowing. As the feed rate increased entering the

shear dominant condition, the feed marks became clearer and the uneven milling phenomenon was reduced, thereby decreasing the surface roughness.

Fig. 12 shows the surface defects of micro-channels under different micro-milling parameters. Experimental results indicated that primary surface defects included feed marks, adhesive material, plastic flow, tearing surface, and
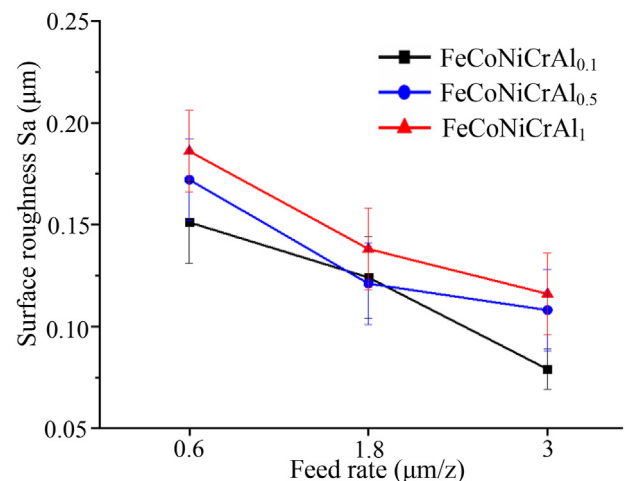

Fig. 11 − 3D surface roughness after micro-milling process.

ploughing grooves. The common surface defect was the evenly distributed feed marks, which was caused by the combined effects of the cutting edge movement and the feed per tooth. Moreover, the feed marks were relatively more obvious under the condition of larger feed rate. As shown in Fig. 12, different degrees and sizes of chips debris adhered to the machined surface. If the adhesive material was crushed and rubbed by the tool surface, the corresponding material smeared was generated on the machined surface. Moreover, side flow and plastic flow were generated due to the squeezing effects of cutting edge and tool surface. The machined surface of $FeCoNiCrAl_{0.1}$ had more side flow and plastic flow due to relatively lower microhardness. Moreover, tearing surface was the common machined surface defects in HEA $FeCoNiCrAl_x$, which usually was related to the formation of built-up edge and unfavorable micro-milling parameters. Under the condition of higher feed rate, the tearing surface was more likely to occur. The topography of tearing surface with different Al element content of HEA $FeCoNiCrAl_x$ was also different, which distinct tear removal phenomena in different phase boundary for $FeCoNiCrAl_1$. Furthermore, many ploughing grooves appeared inside the tearing surface with higher Al element content. Such phenomenon was mainly because $FeCoNiCrAl_1$ had higher microhardness, which might be caused by brittle tearing and micro-chipping on the cutting edge.

Fig. 12(g)—(i) showed the surface topography of the micro-channels on the down milling side and up milling side near the edge burrs, respectively. Near the sides of the micro-channels, the micro-milling tools worked with negative rake angle due to the ploughing effects. Such phenomenon resulted in severe extrusion between the cutting edge and workpiece material, resulting in the plastic flow of the bottom surface material. Moreover, the ploughing grooves and adhesive workpiece materials were more serious. In addition, the surface defects of down milling side were worse than that of up milling side. On the down milling side, large chips fragments were stuck on the machined surface, indicating that the chips on the down milling side were easily broken.

Due to the size effect, the edge burrs in micro-milling were more complicated than that in macro-milling process. Many factors can affect the formation and size of the micro-milling edge burrs, such as material properties, tool geometry and cutting parameters [30]. Due to cost and accuracy limitations, removing burrs through secondary processing was impractical. Fig. 13 presents the edge burrs formed on the micro-channel surfaces under various conditions. The edge burrs of up milling and down milling had different characteristics, which the up milling burrs were small and uneven, while the down milling burrs were larger and wavy. The higher burrs on the down milling side can be explained by that the amount of workpiece material were pushed in front of the cutting edge
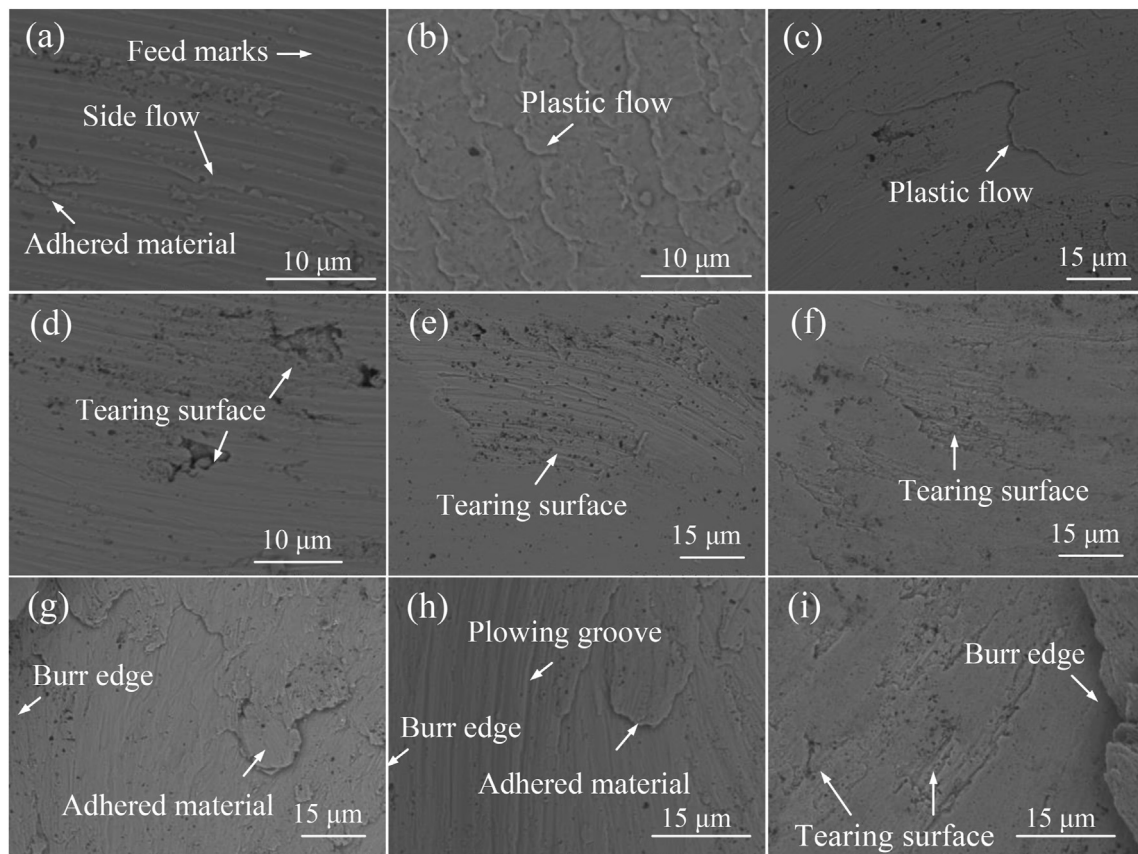

Fig. 12 — Machined surface defects after micro-milling process, (a) $FeCoNiCrAl_{0.1}$, $f_z = 3$ µm/z, (b) $FeCoNiCrAl_{0.1}$, $f_z = 0.6$ µm/z, (c) $FeCoNiCrAl_{0.5}$, $f_z = 0.6$ µm/z, (d) $FeCoNiCrAl_{0.1}$, $f_z = 1.8$ µm/z, (e) $FeCoNiCrAl_{0.5}$, $f_z = 0.6$ µm/z, (f) $FeCoNiCrAl_1$, $f_z = 0.6$ µm/z, (g) $FeCoNiCrAl_{0.5}$, $f_z = 1.8$ µm/z, (h) $FeCoNiCrAl_{0.1}$, $f_z = 1.8$ µm/z, (i) $FeCoNiCrAl_1$, $f_z = 0.6$ µm/z.
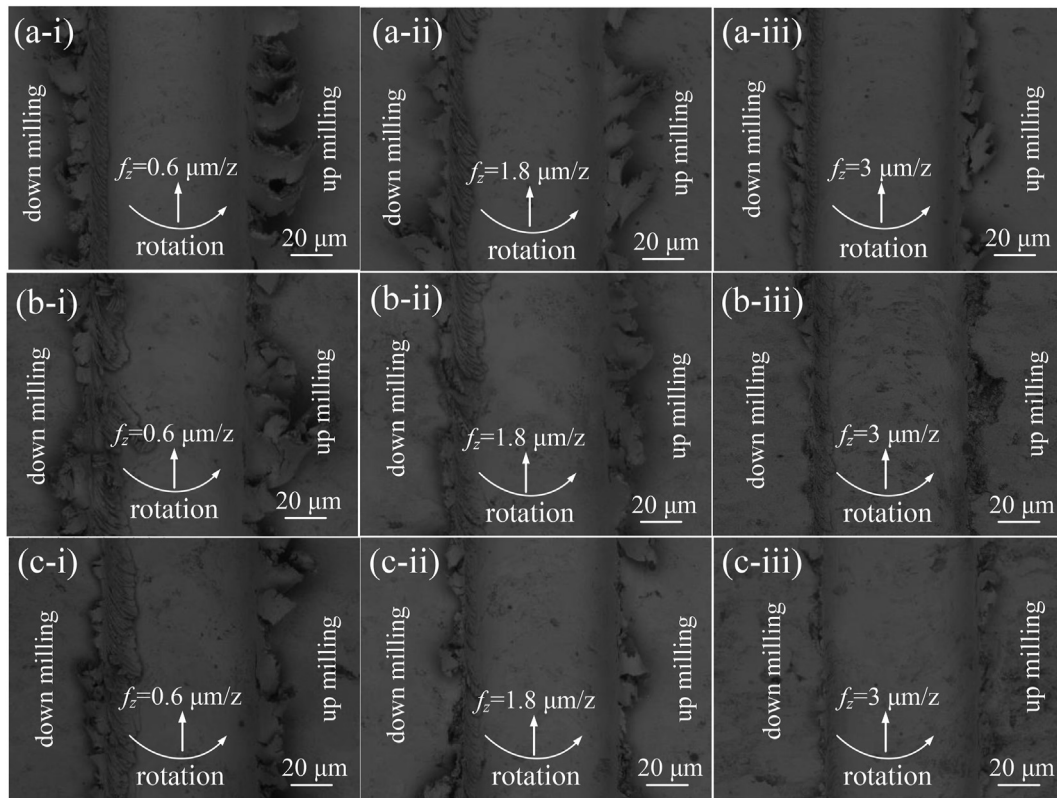
Fig. 13 — Edge burrs morphologies after micro-milling process, (a) FeCoNiCrAl$_{0.1}$, (b) FeCoNiCrAl$_{0.5}$, (c) FeCoNiCrAl$_1$.

along the cutting force direction due to the uncut chip thickness turning from zero to the maximum value with the tool rotating. The average width and size of edge burrs increased as the feed per tooth decreased. This was mostly due to the increased ploughing and friction effects brought by the decreased feed rates, which caused more materials to be squeezed and generate edge burrs during the micro-milling process. Particularly, the edge burrs were relatively reduced because the cutting mechanisms were dominated by shear at the feed per tooth 3 μm/z [31].

Moreover, certain differences of burrs existed in different HEA FeCoNiCrAl$_x$. As shown in Fig. 13, the burrs with lower Al element content were wavy and continuous, while the burrs with higher Al element content were irregular and discontinuous under the same micro-milling parameters. Especially for FeCoNiCrAl$_1$, the edge burrs appeared brittle fracture under the condition of the feed per tooth 3 μm/z. The hardness and microstructure were believed to the main reasons for the differences in burrs formation. Relatively lower microhardness of FeCoNiCrAl$_{0.1}$ was more squeezed to generate wider burrs during micro-milling process. Due to the relatively high microhardness and dual-phase structure of FeCoNiCrAl$_1$, the moment contact between the workpiece and tools was more sensitive to the impact, which might reduce ploughing effects [32].

3.2.3. Chips morphology

The inspection of chip formation and type is an important indicator for understanding metal removal in the micro-milling process. During the micro-milling process, the effective energy consumed by the ploughing zone and the shearing dominant zone affects the chips morphology. Fig. 14 shows the chips morphology of HEA FeCoNiCrAl$_x$ under the different cutting parameters. The chips produced at low feed rates were unstable, indicating that the chip formation mechanism was close to ploughing effect. The shear force for plastic deformation of the chips was insufficient, and the chips produced were mainly short flakes morphology. Under high feed rate, the chip morphology was similar to the shear-dominated process, which presented long and stable periodic sawtooth shape. Moreover, the results of the chips morphology further reflected the different plasticity of HEA FeCoNiCrAl$_x$. With the increase of Al element content, the chips removal mechanism shifted to hard materials, resulting in an increase in chip fragmentation during the shear extrusion process. Especially for FeCoNiCrAl$_1$, the forming of the chips was crushed when it was difficult to be plastically deformed in the cutting process, and the edges and the back of the chips were fractured and cracked.

3.2.4. Tool wear analysis

Figs. 15–17 presents the analysis of tool wear morphologies under different HEA FeCoNiCrAl$_x$. The tool wear analysis indicated that the primary wear modes including flank wear, adhesive workpiece material, built-up edge, fracture, edge chipping, peeling off coating, and grinding marks were observed after micro-milling process. As shown in Fig. 15, the tip of micro-milling tool appeared breakages and fractures under the condition of feed per tooth 0.6 μm/z, which belonged to brittle failure. In this case, the cutting mechanism

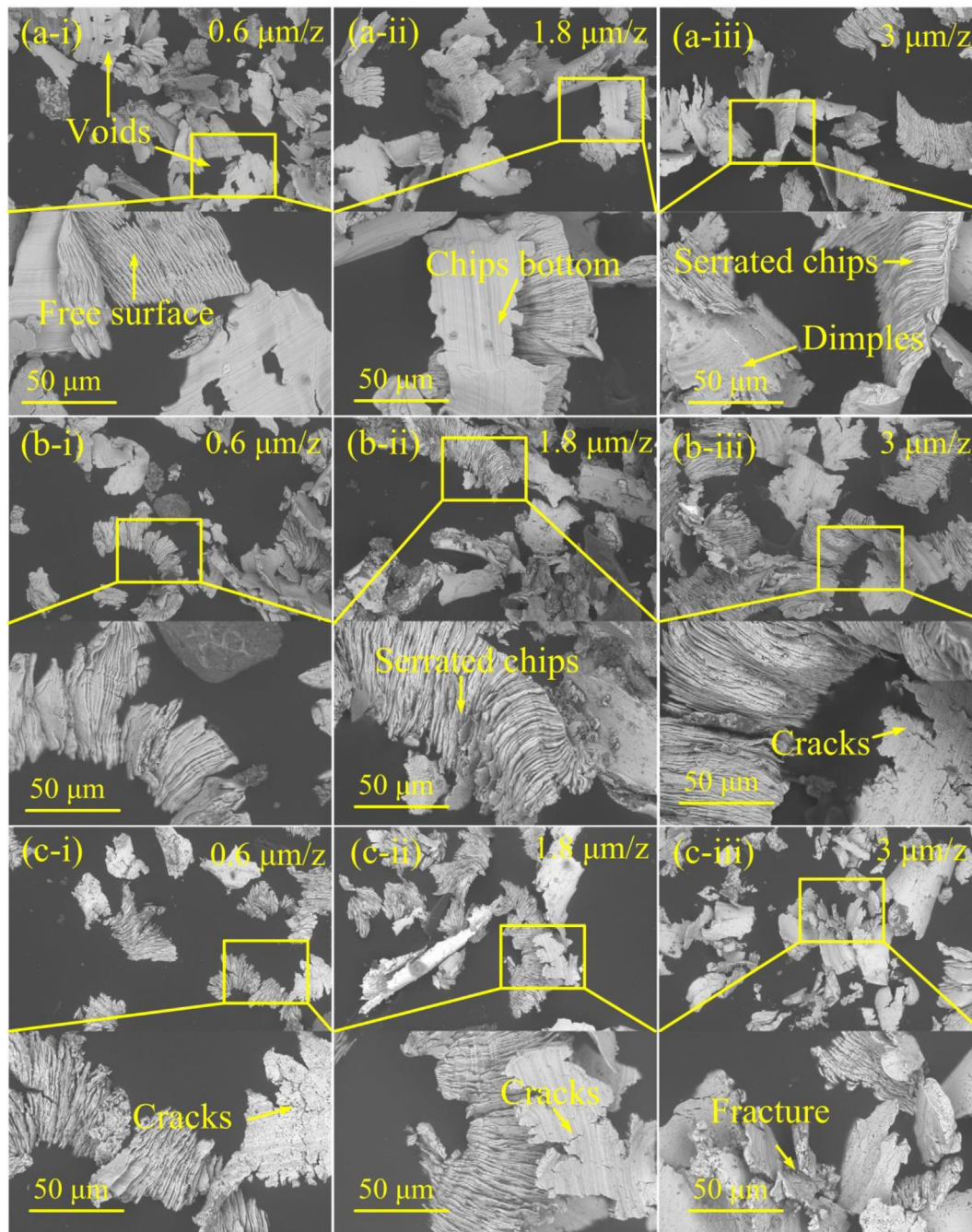**Fig. 14 − Chip morphologies after micro-milling process, (a) FeCoNiCrAl$_{0.1}$, (b) FeCoNiCrAl$_{0.5}$, (c) FeCoNiCrAl$_1$.**

was mainly the ploughing effect, which increased the pressure between workpiece and cutting edge resulting in the cutting edge weakened [33,34]. The adhesion effect of HEA FeCoNiCrAl$_x$ on the tool surface played an important role in determining the cutting performance and tool life, especially in the micro-milling process. As shown in Figs. 15−17, a large amount of HEA FeCoNiCrAl$_x$ was bonded on the tool surface due to the action of extrusion and friction effects. To a certain extent, the adhesive HEA FeCoNiCrAl$_x$ affected the friction conditions at the tool-chip and tool−workpiece interfaces. However, such phenomenon eroded the cutting edge causing severe adhesive wear, which further weaken the cutting edge

and led to catastrophic fracture [35]. It was observed that micro-milling tools appeared more adhesive workpiece material with higher Al element content. This was mainly because the friction and wear were more serious due to higher microhardness [36].

As shown in Figs. 15−17, the adhesive HEA FeCoNiCrAl$_x$ appeared stagnation and accumulation on the cutting edge forming built-up edge (BUE) under the action of extrusion and friction effects. The built-up edge was unstable and easy to break. Such generation and peeling of the built-up edge caused the tool materials in direct contact to be torn, which accelerated tool wear [37]. Since micro-milling was an
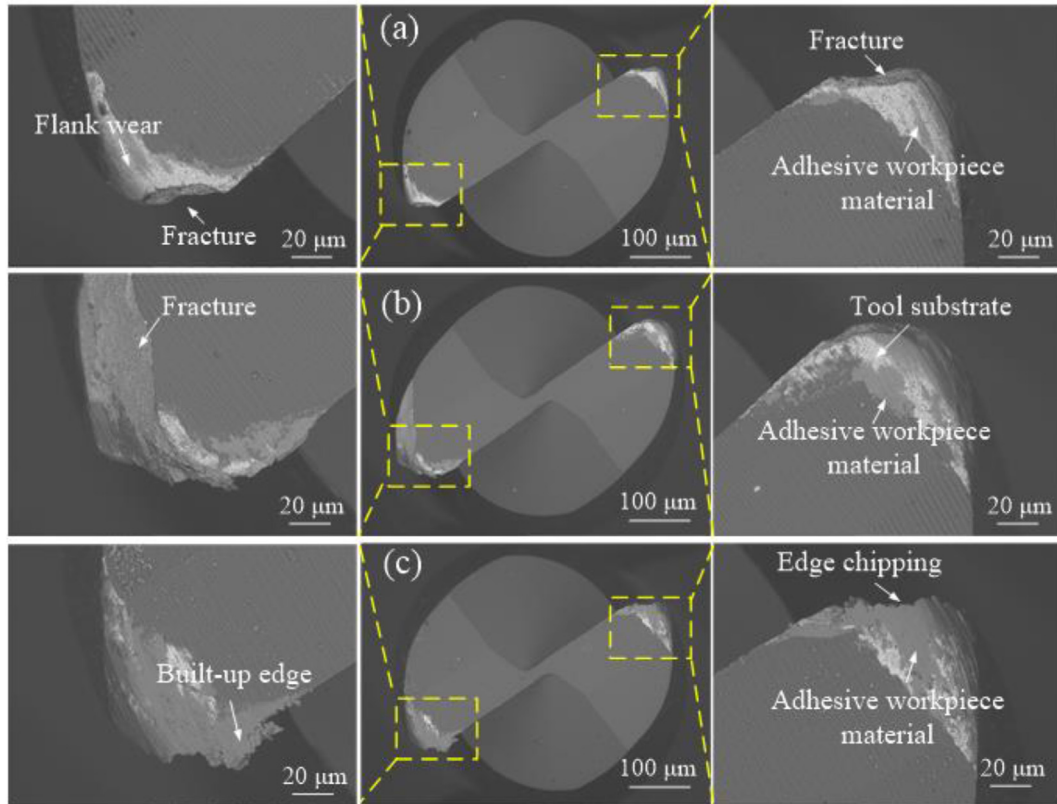
Fig. 15 — Tool wear after micro-milling FeCoNiCrAl$_{0.1}$, (a) $f_z = 0.6$ μm/z, (b) $f_z = 1.8$ μm/z, (c) $f_z = 3$ μm/z.
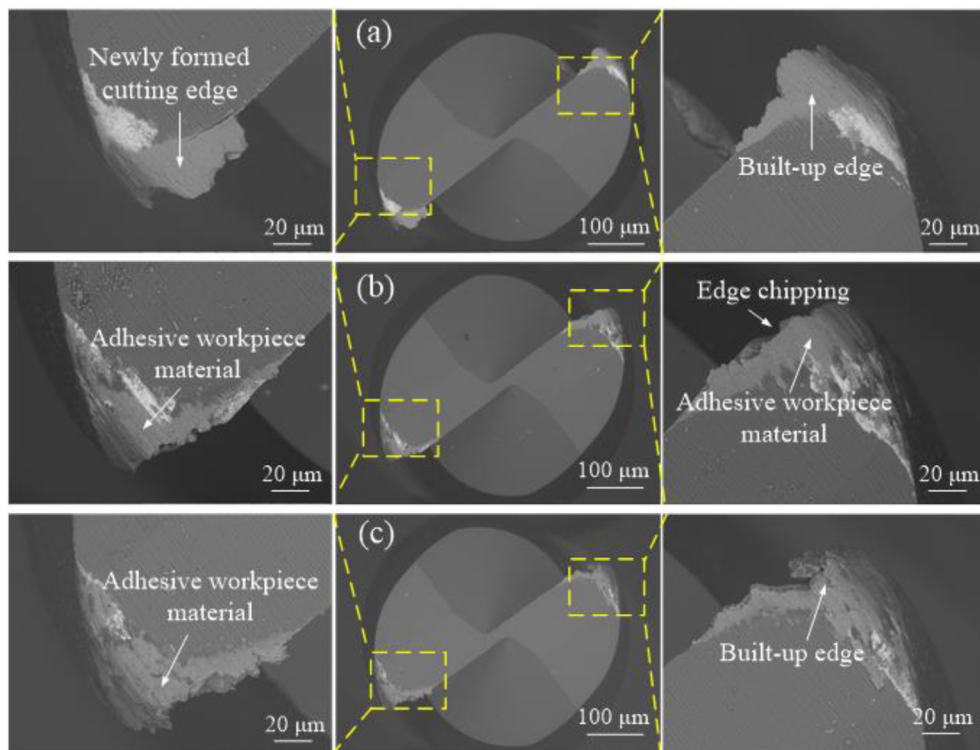
Fig. 16 — Tool wear after micro-milling FeCoNiCrAl$_{0.5}$, (a) $f_z = 0.6$ μm/z, (b) $f_z = 1.8$ μm/z, (c) $f_z = 3$ μm/z.
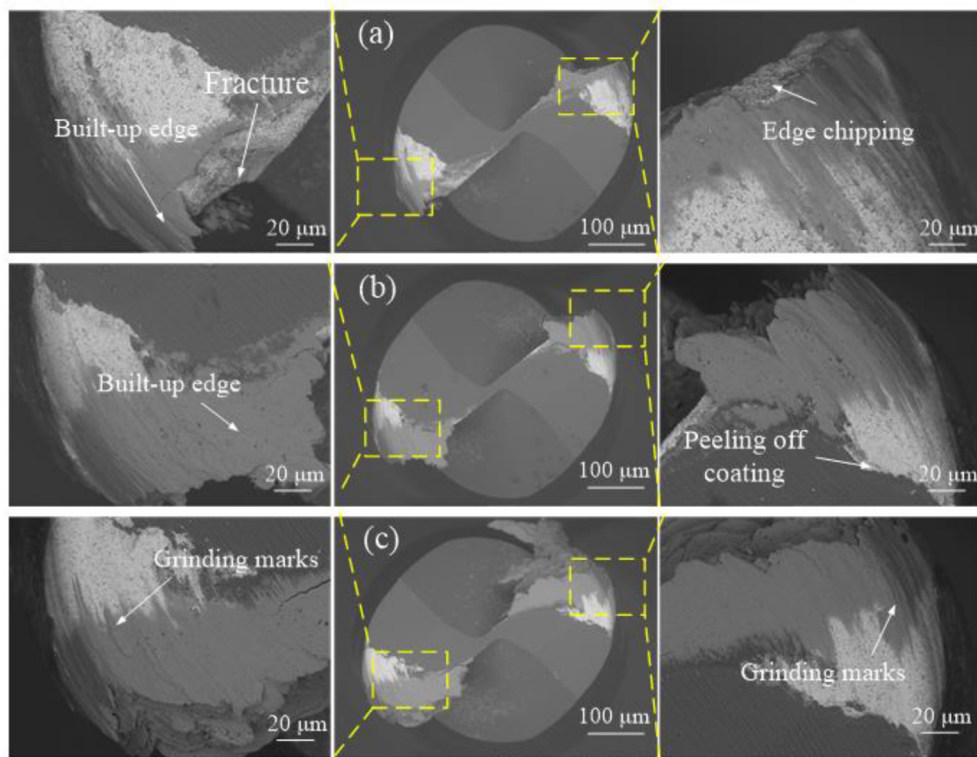
Fig. 17 — Tool wear after micro-milling FeCoNiCrAl$_1$, (a) f_z = 0.6 μm/z, (b) f_z = 1.8 μm/z, (c) f_z = 3 μm/z.

intermittent cutting method, the tensile and compressive stress on the cutting edge alternately changed, the periodic local damage occurred resulting in fatigue damage. As shown in Figs. 15—17, the edge chipping was observed along the tool tip, which caused by high-frequency mechanical impact. In addition, the tool wear was more serious with the increase of the feed per tooth and Al element content, which was due to higher micro-milling heat and greater mechanical loads. Also the increase in Al element content led to increased hardenability and mechanical resistance of HEA FeCoNiCrAl$_x$, which was more likely to produce friction and poor micro-milling performance. The uneven expansion of flank wear and the rapid abrasive wear cause the overall performance of the tool coating to decrease, resulting in coating peeling.

4. Conclusions

The machinability mainly depends on the materials properties and cutting conditions. This work focused on the physical-metallurgical properties and micro-machinability of HEA FeCoNiCrAl$_x$ (x = 0.1, 0.5, 1) with vacuum arc melting preparation. The main conclusions were as follows.

(1) The difference of Al element content affected the element distribution, phase composition, microstructure, and microhardness of HEA FeCoNiCrAl$_x$. The element distribution was relatively uniform for FeCoNiCrAl$_{0.1}$ while the element aggregation occurred in different phases for FeCoNiCrAl$_{0.5}$ and FeCoNiCrAl$_1$. FeCoNiCrAl$_{0.1}$ had single FCC structure while the

coexistence of dual FCC + BCC structure with the gray and white fission biphasic microstructure began to appear for FeCoNiCrAl$_{0.5}$ and FeCoNiCrAl$_1$. The increase of Al element led to the increase of the average microhardness, which the values were 183 HV, 294 HV, and 461 HV for FeCoNiCrAl$_{0.1}$, FeCoNiCrAl$_{0.5}$ and FeCoNiCrAl$_1$, respectively.

(2) The micro-milling forces increased with the increase of Al element content. Compared with FeCoNiCrAl$_{0.1}$ under the condition of 0.6 μm/z, the normal component forces increased by 112.3% and 261.1%, while the feed component forces increased by 45.6% and 159.8% for FeCoNiCrAl$_{0.5}$ and FeCoNiCrAl$_1$, respectively. The specific cutting energy of HEA FeCoNiCrAl$_x$ increased with the increase of Al element content. Especially the specific cutting energy of FeCoNiCrAl$_1$ increased by 152.2%, 115.6%, and 229.8% than that of FeCoNiCrAl$_{0.1}$ under the condition of 0.6 μm/z, 1.8 μm/z, and 3 μm/z, respectively. Moreover, the frequency peak amplitude increased with the decrease of feed rate, and a large peak at the tool-passing frequency enhanced with the increase of Al element content, which mean that the micro-milling process gradually became unstable.

(3) The machined surface with higher Al element content appeared worse surface quality. Especially surface roughness Sa of FeCoNiCrAl$_1$ increased by 23.2%, 11.3%, and 46.8% than that of FeCoNiCrAl$_{0.1}$ under the condition of 0.6 μm/z, 1.8 μm/z, and 3 μm/z, respectively. The reduction in the feed rate resulted in higher surface roughness. Compared with the condition of 0.6 μm/z, surface roughness Sa decreased by 23.2%, 11.3%, and

46.8% under the condition of 3 μm/z for FeCoNiCrAl$_{0.1}$, FeCoNiCrAl$_{0.5}$, and FeCoNiCrAl$_1$, respectively. The distinct tear removal phenomena appeared different phase boundary for FeCoNiCrAl$_1$. The burrs with lower Al content were wavy and continuous while the burrs with higher Al content were irregular and discontinuous. Especially for FeCoNiCrAl$_1$, the burrs appeared brittle fracture under the condition of 3 μm/z.

(4) Tool wear analysis indicated that the primary wear modes including flank wear, adhesive workpiece material, built-up edge, fracture, edge chipping, peeling off coating, and grinding marks were observed after micro-milling process. Tool wear was more serious with the increase of the feed rate and Al element content, which increased hardenability and mechanical resistance resulting in poor micro-milling tool performance.

Declaration of Competing Interest

The authors declare that they have no known competing financial interests or personal relationships that could have appeared to influence the work reported in this paper.

Acknowledgments

REFERENCES

[1] Alaneme KK, Bodunrin MO, Oke SR. Processing, alloy composition and phase transition effect on the mechanical and corrosion properties of high entropy alloys: a review. J Mater Res Technol 2016;5(4):384–93.

[2] Bhandari U, Zhang C, Zeng C, Guo S, Yang S. Computational and experimental investigation of refractory high entropy alloy $Mo_{15}Nb_{20}Re_{15}Ta_{30}W_{20}$. J Mater Res Technol 2020;9(4):8929–36.

[3] Bae JW, Moon J, Jang MJ, Yim D, Kim D, Lee S, et al. Trade-off between tensile property and formability by partial recrystallization of CrMnFeCoNi high-entropy alloy. Mater Sci Eng A 2017;703:324–30.

[4] Lu T, He T, Li Z, Chen H, Han X, Fu Z, et al. Microstructure, mechanical properties and machinability of particulate reinforced Al matrix composites: a comparative study between SiC particles and high-entropy alloy particles. J Mater Res Technol 2020;6:13646–60.

[5] Jiang YQ, Li J, Juan YF, Lu ZJ, Jia WL. Evolution in microstructure and corrosion behavior of AlCoCr$_x$FeNi high-

[6] Masemola K, Popoola P, Malatji N. The effect of annealing temperature on the microstructure, mechanical and electrochemical properties of arc-melted AlCrFeMnNi equiatomic High entropy alloy. J Mater Res Technol 2020;9(3):5241–51.

[7] Yang P, Liu Y, Zhao X, Cheng J, Li H. Electromagnetic wave absorption properties of FeCoNiCrAl$_{0.8}$ high entropy alloy powders and its amorphous structure prepared by high-energy ball milling. J Mater Res 2016;31(16):2398–406.

[8] Zhang H, Wang X, Xu X, Lu Z, Li D. The thermal-mechanical behavior of WTaMoNb high-entropy alloy via selective laser melting (SLM): experiment and simulation. Int J Adv Manuf Technol 2018;96(1–4):461–74.

[9] Soare V, Mitrica D, Constantin I, Popescu G, Csaki I, Tarcolea M, et al. The mechanical and corrosion behaviors of as-cast and re-melted AlCrCuFeMnNi multi-component high-entropy alloy. Metall Mater Trans 2015;46(4):1468–73.

[10] Sun X, Zhu H, Li J, Huang J, Xie Z. Influence of aluminum content on the microstructure and properties of the in-situ TiC reinforced AlxFeCoNiCu high entropy alloy matrix composites. Mater Sci Eng A 2019;743:540–5.

[11] Zhang P, Li Y, Chen Z, Zhang J, Shen B. Oxidation response of a vacuum arc melted NbZrTiCrAl refractory high entropy alloy at 800-1200 C. Vacuum 2019;162:20–7.

[12] Wang C, Tang J, Ou Z, Su G, Ou D, Xia W. Study on microstructure and hardness of AlCoCrCuFeNi-x high-entropy alloy. Foundry Technol 2010;12.

[13] Jiang H, Huang TD, Su C, Zhang HB. Microstructure and mechanical behavior of CrFeNi2V0.5Wx (x=0, 0.25) high-entropy alloys. Acta Metall Sin 2020:1–7.

[14] Guo J, Goh M, Zhu Z, Lee X, Nai MLS, Wei J. On the machining of selective laser melting CoCrFeMnNi high-entropy alloy. Mater Des 2018;153:211–20.

[15] Clauß B, Liborius H, Lindner T, Lobel M, Schubert A, Lampke T. Influence of the cutting parameters on the surface properties in turning of a thermally sprayed AlCoCrFeNiTi coating. Proc CIRP 2020;87:19–24.

[16] Liborius H, Uhlig T, Clauß B, Nestler A. Influence of the cutting material on tool wear, surface roughness, and force components for different cutting speeds in face turning of CoCrFeNi high-entropy alloys. IOP Conf Ser Mater Sci Eng 2021;1147(1):012008.

[17] Litwa P, Hernandez-Nava E, Guan D, Goodall R. The additive manufacture processing and machinability of CrMnFeCoNi high entropy alloy. Mater Des 2021;198:109380.

[18] Constantin G, Balan E, Voiculescu I, Geanta V. Cutting behavior of Al0.6CoCrFeNi high entropy alloy. Materials 2020;13(18):4181.

[19] Huang Z, Dai Y, Li Z, Zhang G, Chang C, Ma J. Investigation on surface morphology and crystalline phase deformation of Al80Li5Mg5Zn5Cu5 high-entropy alloy by ultra-precision cutting. Mater Des 2020;186:108367.

[20] Richter T, Schröpfer D, Rhode M, Borner A. Influence of modern machining processes on the surface integrity of high-entropy alloys. IOP Conf Ser Mater Sci Eng 2020;882(1):012016.

[21] Aslantas K, Hopa HE, Percin M, Ucun I, Cicek A. Cutting performance of nano-crystalline diamond (NCD) coating in micro-milling of Ti6Al4V alloy. Precis Eng 2016;45:55–66.

[22] Wang Y, Zou B, Wang J, Wu Y, Huang C. Effect of the progressive tool wear on surface topography and chip formation in micro-milling of Ti-6Al-4V using Ti (C7N3)-based cermet micro-mill. Tribol Int 2020;141:105900.

[23] Mouralova K, Benes L, Prokes T, Zahradnicek R, Bednar J, Otoupalik J, et al. Micro-milling machinability of pure molybdenum. Int J Adv Manuf Technol 2019;102(9):4153–65.

[24] Rezaei H, Sadeghi MH, Budak E. Determination of minimum uncut chip thickness under various machining conditions during micro-milling of Ti-6Al-4V. Int J Adv Manuf Technol 2018;95(5):1617–34.

[25] Hojati F, Daneshi A, Soltani B, Azarhoushang B. Study on machinability of additively manufactured and conventional titanium alloys in micro-milling process. Precis Eng 2020;62:1–9.

[26] Teng X, Huo D, Wong E, Meenashisundaram G, Gupta M. Micro-machinability of nanoparticle-reinforced Mg-based MMCs: an experimental investigation. Int J Adv Manuf Technol 2016;87(5):2165–78.

[27] Wang Y, Zou B, Huang C, Liu Z, Yao P. The micro-cutting performance of cermet and coated WC micro-mills in machining of TC4 alloy micro-grooves. Int J Adv Manuf Technol 2018;96(1):1403–14.

[28] Yao Y, Zhu H, Huang C. Investigation on chip formation and surface integrity in micro end milling of maraging steel. Int J Adv Manuf Technol 2019;102(5):1973–84.

[29] Ray D, Puri AB, Hanumaiah N. Experimental analysis on the quality aspects of micro-channels in mechanical micro milling of Zr-based bulk metallic glass. Measurement 2020;158:107622.

[30] de Oliveira Campos F, Araujo AC, Munhoz ALJ. The influence of additive manufacturing on the micromilling machinability of Ti6Al4V: a comparison of SLM and commercial workpieces. J Manuf Process 2020;60:299–307.

[31] Sorgato M, Bertolini R, Bruschi S. On the correlation between surface quality and tool wear in micro-milling of pure copper. J Manuf Process 2020;50:547–60.

[32] Silva LC, da Silva MB. Investigation of burr formation and tool wear in micromilling operation of duplex stainless steel. Precis Eng 2019;60:178–88.

[33] Liang X, Liu Z, Wang B. State-of-the-art of surface integrity induced by tool wear effects in machining process of titanium and nickel alloys: a review. Measurement 2019;132:150–81.

[34] Shakoori N, Fu G, Le B, Khalig J, Jiang L, Huo D. An experimental investigation on tool wear behaviour of uncoated and coated micro-tools in micro-milling of graphene-reinforced polymer nanocomposites. Int J Adv Manuf Technol 2021;113(7):2003–15.

[35] Liang X, Liu Z. Tool wear behaviors and corresponding machined surface topography during high-speed machining of Ti-6Al-4V with fine grain tools. Tribol Int 2018;121:321–32.

[36] Gao Q, Guo G, Cai M. Wear mechanism and experimental study of a tool used for micro-milling single-crystal nickel-based superalloys. Int J Adv Manuf Technol 2021;113(1):117–29.

[37] Wang Y, Zou B, Huang C. Tool wear mechanisms and micro-channels quality in micro-machining of Ti-6Al-4V alloy using the Ti (C7N3)-based cermet micro-mills. Tribol Int 2020;134:60–76.